Metallography, Microstructure, and Analysis (2019) 8:607–622
https://doi.org/10.1007/s13632-019-00569-6

TECHNICAL ARTICLE

Tribological Damage Characteristics of a Novel Low Carbon Steel Synthesized Through Intercritical Thermal Cycling

Amir Raza Subhani[1] · Dipak Kumar Mondal[1] · Joydeep Maity[1]

Received: 21 February 2019 / Revised: 6 July 2019 / Accepted: 28 August 2019 / Published online: 13 September 2019

Abstract

Enhanced hardness development in an intercritical thermal-cycled steel as compared to conventional-annealed low carbon steel is critically introspected with the study of dry sliding wear behavior (at sliding speed ~ 1 ms^{-1}, load range: 4.9–14.71 N) in view of readily awaited in-depth correlation between wear mechanism and structural evolution. The steel in annealed condition (possessing lower hardness) suffers from higher wear loss (inferior resistance against wear) with respect to the steel subjected to intercritical thermal cycling, except at highest load (14.71 N). This is primarily due to the removal of layers of oxide and harder pearlite regions primarily through abrasion. Intercritical thermal-cycled steel significantly resists wear loss up to 9.81 N load and provides much superior wear resistance than annealed steel. However, at highest load (14.71 N), the softening effect in the form of tempering coupled with microplowing abrasion results in an aggravated wear loss in this steel.

Keywords AISI 1010 steel · Intercritical thermal cycling · Dry sliding wear test · Oxidation, microcutting, and microplowing · Strain hardening and martensite tempering · Wear resistance

Introduction

Steel is considered to be the most significant material in progress of human civilization since Iron Age. In modern era, there has been an enhanced demand of new-generation hard and wear-resistant materials specifically for structural applications where machine parts are in relative motion. Although unalloyed steel containing lower proportion of carbon (≤ 0.2 mass% C) is a cost-effective engineering material, it suffers from poor wear resistance and hardness [1]. By virtue of relatively lower volume fraction of pearlite in the microstructure in annealed condition, unalloyed annealed low carbon steel (an aggregate of α-ferrite and pearlite) exhibits poor wear resistance. Hard cementite phase in pearlite (a lamellar phase mixture of α-ferrite and cementite) provides significant resistance to wear loss [2–4]. Indeed, the tribological damage of steel in view of techno-scientific perspective in all its details (mechanism of wear and associated microstructure evolution) is a difficult task to deal with. The wear mechanism in steel incorporates various aspects, namely strain hardening, adhesive bond formation, evolution of oxide, abrasion, and associated microstructural modifications [5]. The ambiguity persists in existing literature in correlating hardness, microstructure (sole or combined microconstituents) and wear resistance of steel. In this regard, despite 'bainite' being a much harder microconstituent, an inferior wear resistance of bainitic steel as compared to pearlitic has been reported [6]. In the absence of lamellar morphology, bainite suffered from intense adhesive wear and associated plastic deformation. The superior wear resistance of pearlite was exemplified with adherent (thereby wear-resistant) surface oxide generation by virtue of a prolong oxidative wear regime [7–9]. Such an observation was well supported by Lee and Polycarpou [10] in view of a low work hardening rate of lower bainite. It was found that the initially softer pearlitic rail steel was work hardened more than the initially harder bainitic rail steel as in-service stresses accumulated on the rails, and thus exhibited a better wear resistance [10]. In a contradictory observation, Xu and Kennon [11] reported bainitic structure to possess the maximum resistance to wear followed by tempered martensite and annealed structure while carrying out two-body abrasion tests on plain carbon steels over a wide range of compositions (0.10–1.4 wt.%C). Spheroidized structure was

✉ Joydeep Maity
joydeep_maity@yahoo.co.in

[1] Department of Metallurgical and Materials Engineering, National Institute of Technology Durgapur, Durgapur, West Bengal 713209, India

found to possess the lowest wear resistance. Again, Kalousek et al. [12] observed an enhanced wear resistance of pearlite with respect to tempered martensite or bainite in Cr–Mo steel. This was explained in terms of a considerable strain hardening of pearlite. Besides, oxide evolution at surface of nano-structured Hadfield manganese steel provides much superior wear resistance as compared to conventional Hadfield manganese steel [13].

Therefore, comparative investigation of wear behavior in view of chemical composition, microstructure, and processing parameters is very much necessary for application of steels in real practice [14]. Adopting right processing methodology, either matrix is strengthened [15] or hard particles are embedded in existing matrix to enhance wear resistance [16–18]. Apart from hard particle (such as cementite) being in situ evolved through solid-state phase transformation, it may be incorporated through various processing routes as well. In this regard, recent studies on surface alloying of steel with Cr by high current pulsed electron beam treatment [16], incorporation of hard TiC particles through tungsten inert gas torch technique [17] and plasma nitriding followed by aluminizing (so as to evolve hard AlN particles) of AISI 1045 steel [18] to enhance wear resistance are noteworthy to mention.

In this work, realizing the limitations of unalloyed low carbon annealed steel in view of low wear resistance and hardness, solid-state microstructural synthesis of AISI 1010 steel is carried out with four thermal cycles, where each cycle involves a short-duration holding in the intercritical temperature domain followed by ice brine quenching. Tribological damage characteristic of this novel microstructure is introspected in comparison with the annealed one. The novelty of this research work is envisaged with: (1) new microstructure evolution to provide much higher hardness and wear resistance as compared to annealed condition and (2) in-depth correlation between wear mechanism and structural evolution.

Fig. 2 FESEM micrographs of ITC-4Cy representing (**a**) overall microstructures, (**b**) martensite matrix, (**c**) nano-sized cementite particle in martensite matrix and its (**d**) EDS spectra, (**e**) nano-sized cementite particle in α-ferrite island and its (**f**) EDS spectra; (**g**) FEG-TEM micrograph showing nano-sized cementite particle-enriched region of α-ferrite island along with SADP ▶

Experimental Procedure

Material, Thermal Treatment, and Characterization

Bars of AISI 1010 steel (0.103 mass% C, 0.406 mass% Mn, 0.037 mass% P, 0.042 mass% S, remaining Fe) were provided with homogenizing annealing treatment (1100 °C, 2-h holding, furnace cooling; specimen code: AN). Thereafter, one set of the annealed steel bars was provided with intercritical thermal cycling for four cycles (specimen code: ITC-4Cy). Successive thermal steps for each cycle are: (1) holding at an intercritical temperature of 810 °C [between A_1 temperature (715 °C) and A_3 temperature (845 °C)] for a little span (6 min) and (2) ice-brine quench. A_3 and A_1 temperatures were ascertained (so as to select intercritical temperature) using standard formula provided in the literature [19]. The measured hardness values for five successive cycles were 312 ± 3, 317 ± 2, 324 ± 3, 464 ± 8, and 234 ± 6 HV, respectively. The number of cycles of heat treatment was considered up to 'four' for present investigation in view of the highest hardness value (464 ± 8 HV) obtained. Metallographic specimens prepared from heat-treated bars were studied with field emission scanning electron microscope (FESEM) and high-resolution transmission electron microscope equipped with field emission gun (FEG-TEM). Besides, Vickers bulk hardness (at 30 Kgf load) and Vickers microhardness (at 25–100 gf load) tests were also performed on heat-treated specimens.

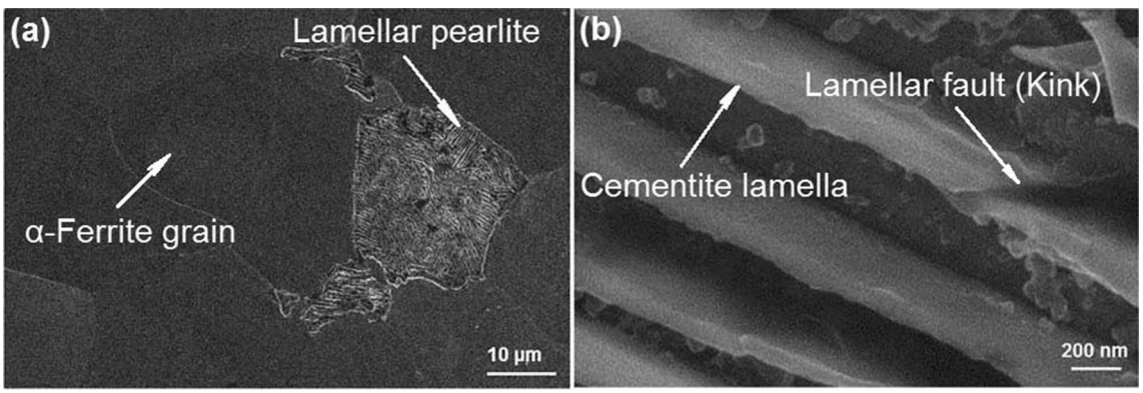

Fig. 1 FESEM micrographs of AN representing (**a**) overall microstructure and (**b**) presence of lamellar fault in the form of kink

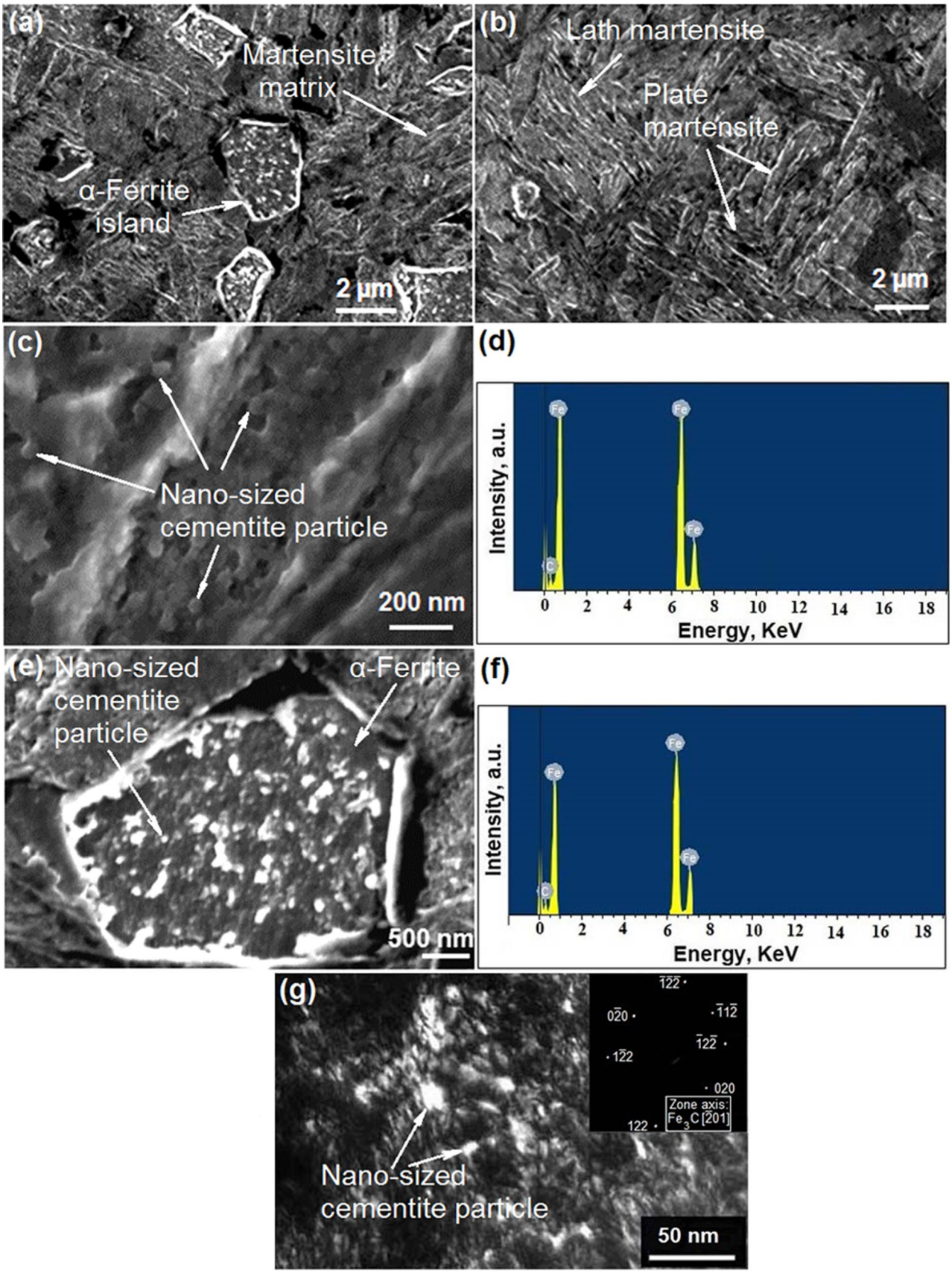
(a)
Martensite matrix
α-Ferrite island
2 μm
(b)
Lath martensite
Plate martensite
2 μm
(c)
Nano-sized cementite particle
200 nm
(d)
Intensity, a.u.
Energy, KeV
(e)
Nano-sized cementite particle
α-Ferrite
500 nm
(f)
Intensity, a.u.
Energy, KeV
(g)
Zone axis: Fe3C [201]
Nano-sized cementite particle
50 nm

Wear Test and Subsequent Material Characterization

Cylindrical pin (7 mm Ø × 20 mm)-shaped specimens were machined out from steel bars after heat treatment and subjected to tribological damage evaluation in tribometer of pin-on-disk type under dry sliding condition. Alumina disk (hardness = 2600 HV [20]) was used as counter material rotating at 200 rpm. Wear track diameter, sliding speed, total test time, and total sliding distance were fixed at 0.1 m, 1.047 m s^{-1}, 5400 s, and 5653.8 m, respectively. 'Normal load' (*P*), the main process variable, is varied at four values, viz. 4.9 N, 7.35 N, 9.81 N, and 14.71 N. In accordance with the loads applied, the pressures were 0.13, 0.19, 0.26, and 0.38 MPa, respectively, for a pin cross-sectional area of 38.48×10^{-6} m^2. The load range was selected with regard to literature survey [6] on wear test of various steels. Since 'wear' is a surface phenomenon and atoms at surface are more mobile than interior, in the presence of very hard abrasive counter material (alumina in the present investigation), the load range chosen was sufficient to introspect tribological surface damage phenomena. Wear test data were used to generate cumulative wear loss (CWL) versus sliding distance (SD) and coefficient of friction (COF) versus sliding distance (SD) plots. Weight loss of specimen pin on completion of wear test was measured to evaluate overall tribological damage as suggested in the literature [6]. On completion of wear test, worn surface (as is and polished and etched) and worn debris were studied with FESEM along with EDS analysis. Worn surfaces were further introspected with XRD analysis.

Results and Discussion

Evolved Microconstituents

The evolved structure in annealed AISI 1010 steel (AN) corroborates primarily the proeutectoid α-ferrite and lamellar pearlite (Fig. 1a). Notably, 'lamellar fault' sites [21] are observed in cementite lamella of pearlite (Fig. 1b). The microhardness values of the α-ferrite matrix region and pearlite region are measured as 119 ± 3 HV and 177 ± 11 HV, respectively. The measured bulk hardness of AN (124 ± 2 HV) is quite low due to abundance of α-ferrite region in the microstructure. The new steel developed through intercritical thermal cycling (specimen code: ITC-4Cy) possesses a structure that is comprised of α-ferrite islands (contained with nano-cementite dispersion) in martensite (also contained with dispersed nano-cementite) (Fig. 2a). Both 'lath' and 'plate' morphologies are exhibited by the martensite matrix (Fig. 2b). Furthermore, dispersed nano-cementite particles (size range = 33–62 nm) are found to be present in martensite matrix (Fig. 2c). Besides, α-ferrite islands also contain dispersed nano-cementite (size range = 38–85 nm) (Fig. 2d). Nano-cementite particles dispersed in α-ferrite island are also identified in FEG-TEM micrograph (Fig. 2e). Holding at intercritical temperature domain evolves two-phase austenite plus α-ferrite structure. Upon ice-brine quenching, austenite transforms to martensite resulting in simultaneous presence of martensite and α-ferrite. Besides, repeated short-duration holding at intercritical domain results in fragmentation of cementite lamella (present in pearlite of initial microstructure) through preferential dissolution of cementite lamella at lamellar fault sites [22]. With short-duration holding being repeated many times (causing repeated lamellar fragmentation), nano-sized cementite particles are originated where very fast rate of cooling in ice brine restricts divorced eutectoid growth of cementite particles during cooling. Refinement of cementite, as a consequence of pearlite decomposition, is due to so-called lamellar fragmentation on repeated thermal cycling, mechanism of which has been established by present corresponding

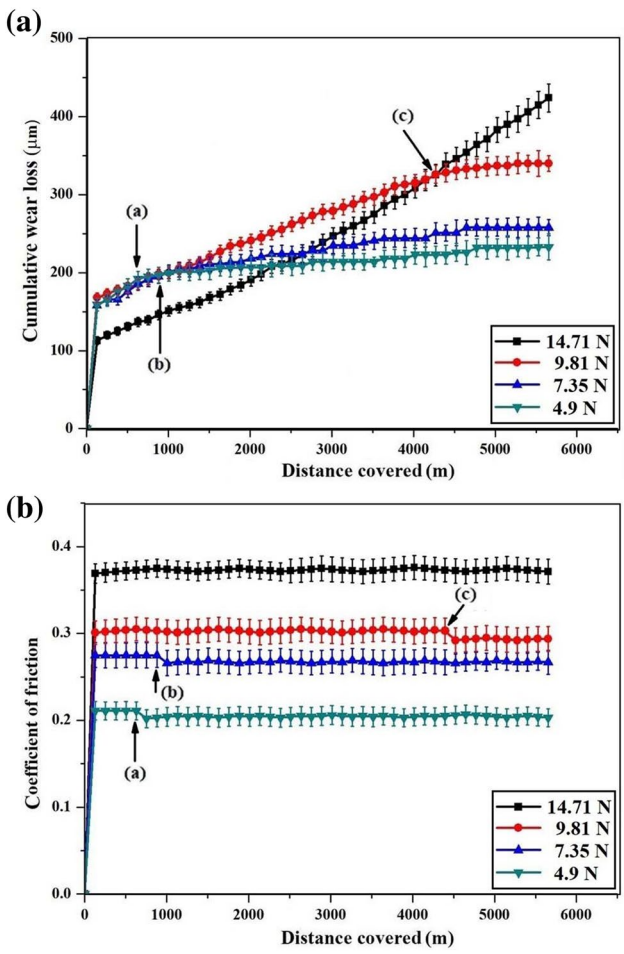

Fig. 3 Wear test results for AN showing (**a**) cumulative wear loss and (**b**) coefficient of friction

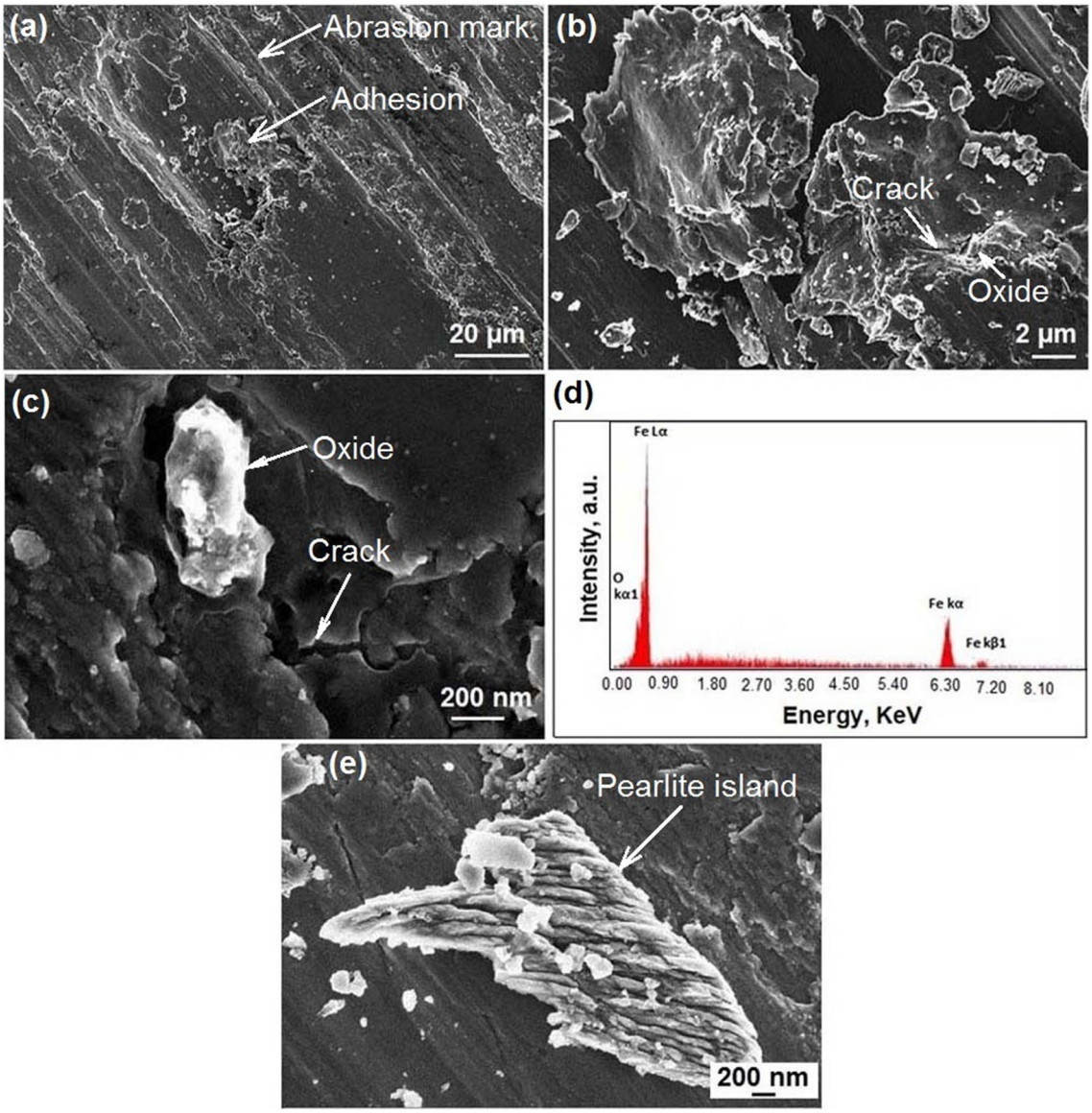

Fig. 4 FESEM micrographs of the worn surface of AN subjected to 4.9 N load: (**a**) overall appearance; (**b**) adhesion region; (**c**) crack nucleation at oxide/metallic matrix interface; (**d**) EDS spectra of oxide; and (**e**) pearlite island

author [22]. Lamellar fragmentation primarily occurs due to atomic diffusion from lamellar fault site to adjacent austenite matrix as well as to adjacent flat surface of cementite lamella. Furthermore, the refinement of matrix phases (α-ferrite or martensite) is primarily due to short-duration holding in each step that ceases growth (duration of holding being small). The measured individual microhardness values of nano-cementite-dispersed α-ferrite island, lath martensite region, and plate martensite region are 332 ± 4 HV, 509 ± 7 HV, and 610 ± 16 HV, respectively. The measured bulk hardness of ITC-4Cy (464 ± 8 HV) is much higher than that of AN (124 ± 2 HV) due to the presence of dispersed nano-cementite and hard martensite phases.

Tribological Damage Mechanism

Investigation of the process of tribological surface damage in steel under load is a critical task due to contribution of many counteracting phenomena, namely (1) material removal processes (adhesion, subsurface cracking and delamination,

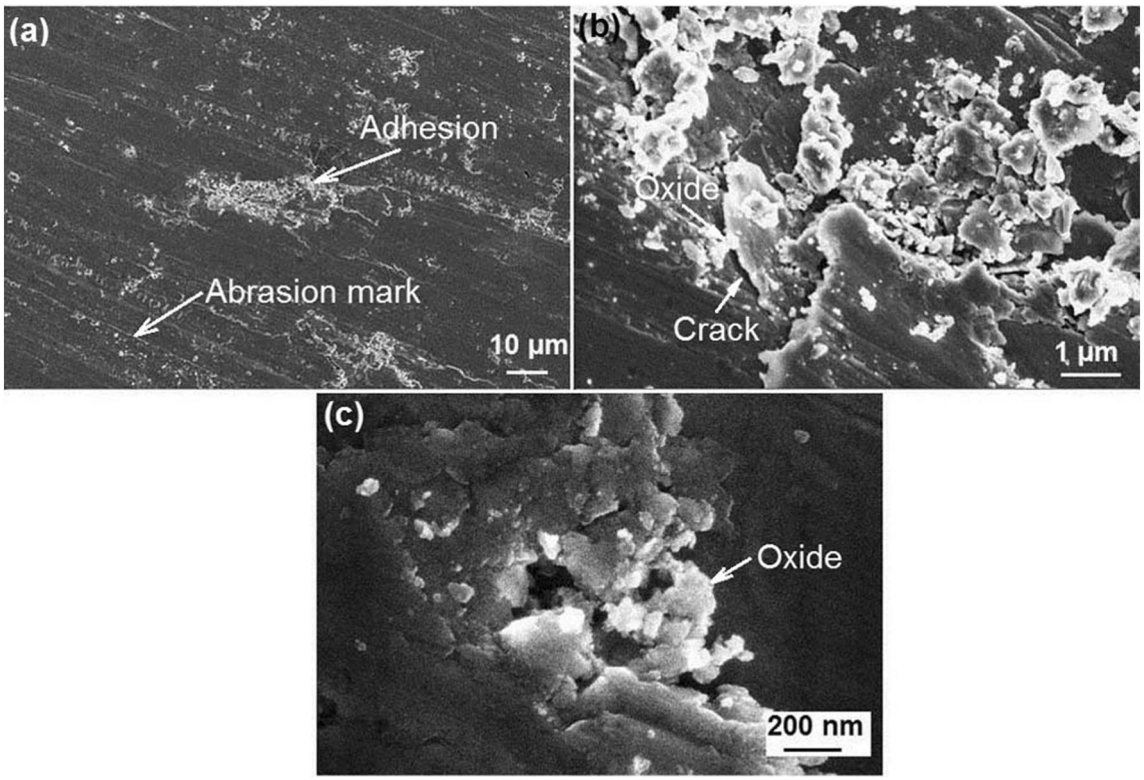

Fig. 5 FESEM micrographs of the worn surface of AN subjected to 7.35 N load: (**a**) overall appearance; (**b**) adhesion region; and (**c**) oxide evolution

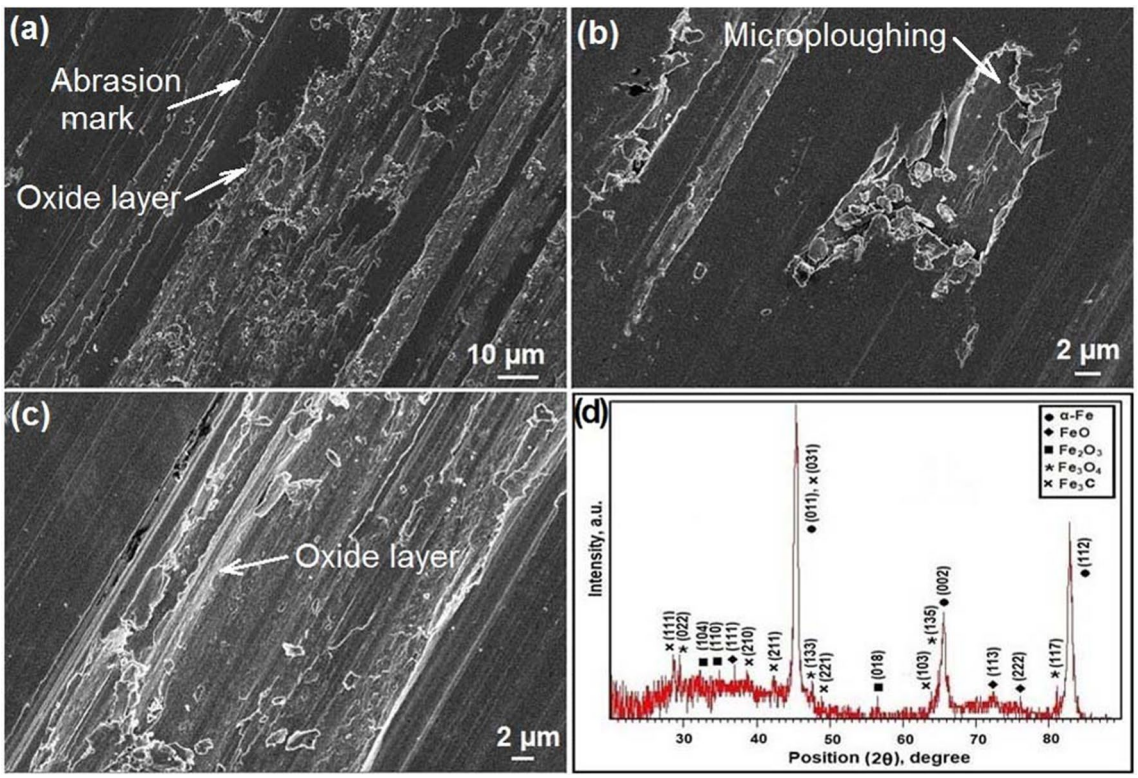

Fig. 6 FESEM micrographs of the worn surface of AN subjected to 9.81 N load: (**a**) overall appearance; (**b**) microplowing effect; (**c**) oxide layer; and (**d**) XRD analysis of worn surface

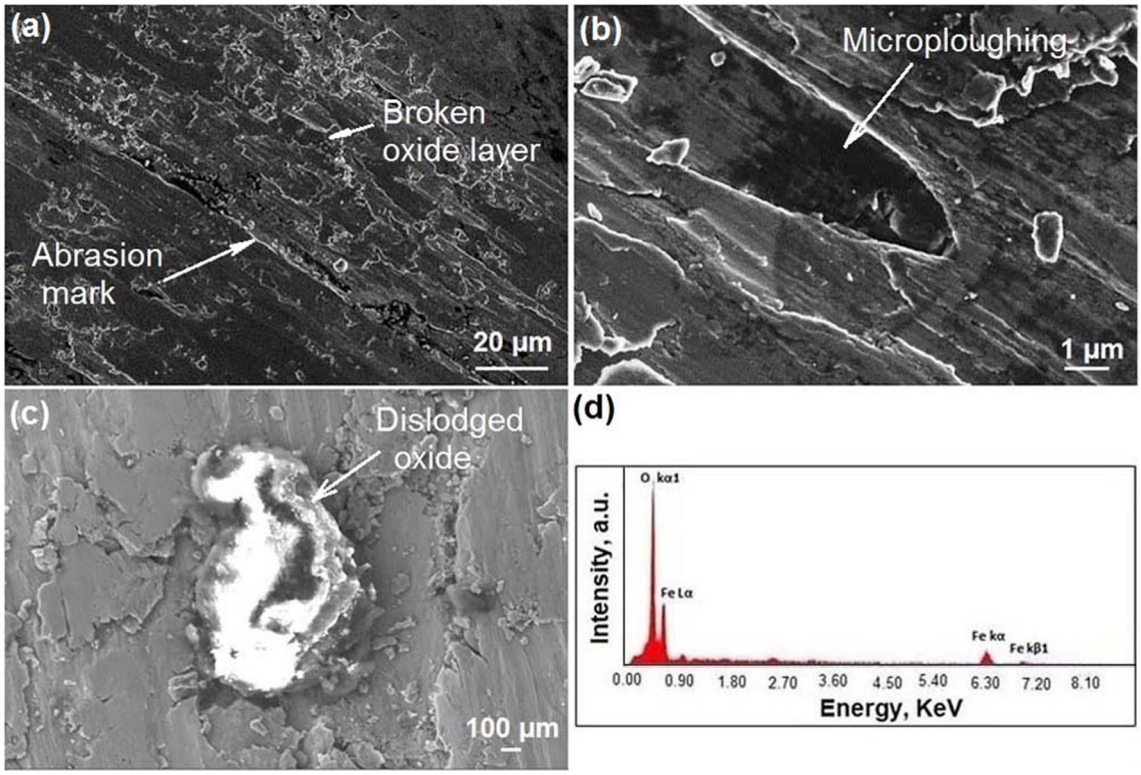

Fig. 7 FESEM micrographs of the worn surface of AN subjected to 14.71 N load: (**a**) overall appearance; (**b**) microplowing effect; (**c**) dislodged oxide particle; and its (**d**) EDS spectra

microcutting and microplowing effects of abrasion, etc.), (2) frictional heating of surface and environmental interaction (oxidation), and (3) surface strain hardening. The progress of tribological damage on linear scale is scientifically studied with regard to CWL in correlation with the variation of COF with SD. In connection with these aspects, the features observed on worn surface and in worn debris envisage primary wear mechanism. This is emphasized in the next part of discussion. Strain hardening aspects are focused upon in later part through investigation of polished and etched worn surface so as to understand overall wear behavior.

Tribological Damage in Annealed Steel

Figure 3a, b depicts experimentally obtained plots representing CWL and COF for annealed steel (AN). At lowest load (4.9 N), the tribological damage rises steadily with SD till point 'a' (Fig. 3a); henceforth, it slows down. In accordance with this behavior, the COF (Fig. 3b) exhibits steady nature till point 'a' and falls afterward. At 4.9 N, the overall surface after wear test exhibits prominent features of adhesion along with marks of abrasion (Fig. 4a).

In the adhesion region, localized adhesion bonds are developed between pin surface and counter material. These bonds are consequently broken down through strain hardening forming cracks. The crack growth connecting one another results in so-called delamination, where the metal sheet is detached from the surface [23]. This is evident in Fig. 4b.

Evolution of iron oxide is exemplified with FESEM micrograph and EDS analysis (Fig. 4c and d). Besides, marks of abrasion exemplify microcutting mechanism of abrasive wear (Fig. 4a). Accordingly, till point 'a' (Fig. 3a and b), a sluggish but steady tribological damage occurs via conjoint adhesive and abrasive wear. Afterward, the process of wear is inhibited by oxide evolution. Besides, pearlite island (harder microconstituent) is found to stand tall so as to resist wear loss as well (Fig. 4e).

At 7.35 N, evidences of conjoint adhesive wear and abrasive wear are visible (Fig. 5a). Adhesion zone exhibits breakdown of adhesive joint, oxide generation, crack nucleation, and metal sheet removal (Fig. 5b). As a consequence, CWL rises with SD till point 'b' (Fig. 3a). Afterward, oxide evolution inhibits tribological damage (Fig. 5c). Accordingly, COF decreases after point 'b'.

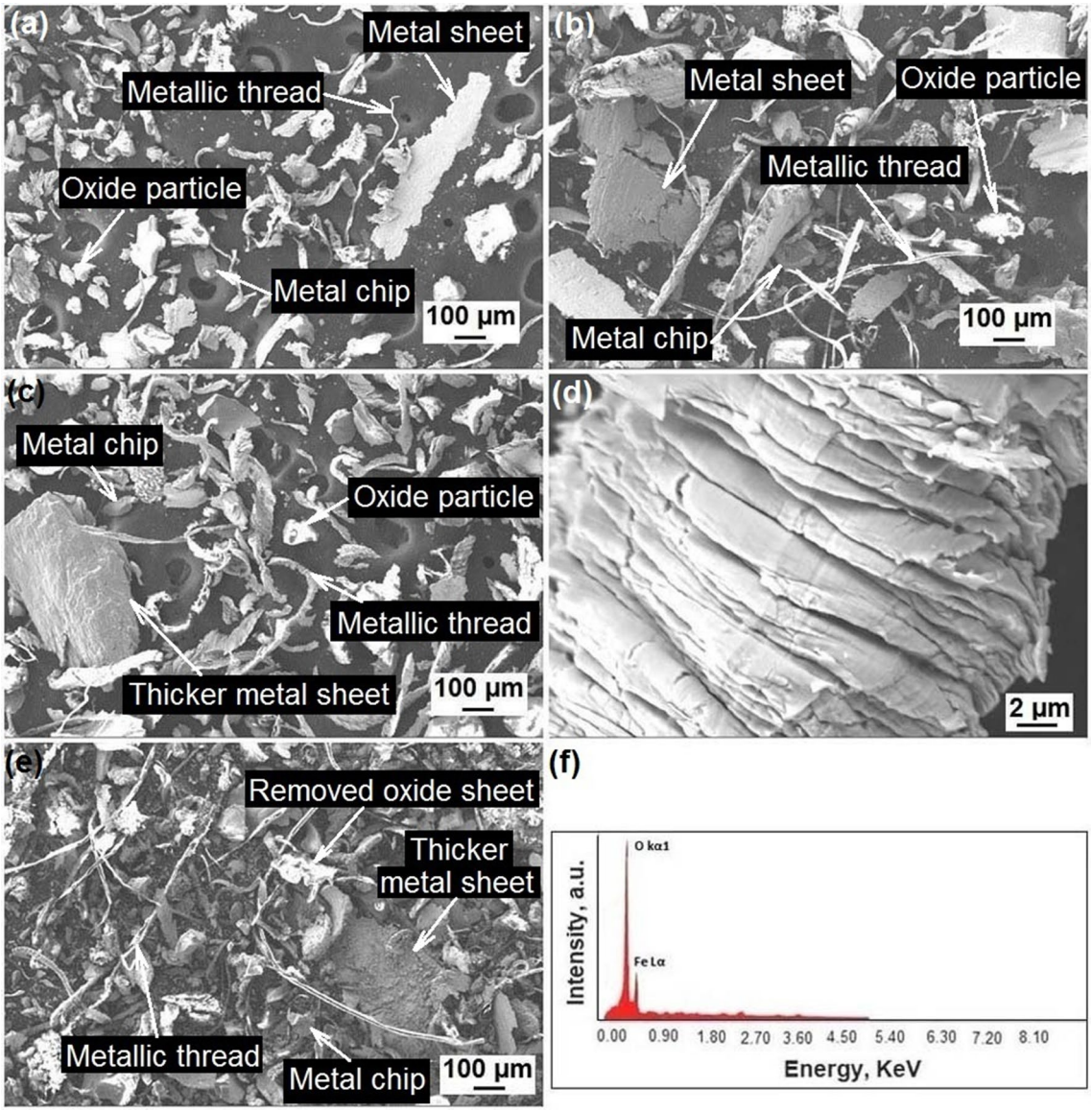

Fig. 8 FESEM micrographs of the worn debris of AN at different loads, namely (**a**) 4.9 N, (**b**) 7.35 N, (**c**) 9.81 N (overall micrograph), (**d**) 9.81 N (lamellar pearlite), and (**e**) 14.71 N, (**f**) FESEM-based EDS spectra of oxide sheet removed at 14.71 N load

The characteristic CWL plot at 9.81 N load reflects an accelerated tribological damage till point 'c' and subsequent arrest in CWL (Fig. 3a). In concurrence, COF falls beyond point 'c' on inhibition of wear. The pin surface mainly corroborates distinct marks of abrasion and evolution of oxide layer (Fig. 6a). The marks of abrasion envisage microcutting action of counter material. Apart from microcutting mechanism, more severe abrasive action in the form of microplowing is also evident with generation of 'ditch' (Fig. 6b). Accordingly, until point 'c,' extensive wear loss takes place, and afterward, evolution of oxide layer (Fig. 6c and d) impedes the tribological damage process due to lubricating effect of oxide [24]. Figure 6d identifies relevant phases through X-ray diffraction analysis. It is well known that X-ray diffraction does not occur ideally in real experimental situation. Therefore, the closely spaced strongest peaks of cementite (at $2\theta = 45.014°$) and α-Fe (at $2\theta = 44.680°$) are found to be overlapped.

Tribological damage characteristics at peak load (14.71 N) exemplify a steady surface damage (Fig. 3a). Accordingly, the COF remains almost steady (Fig. 3b). The surface of wear tested specimen corroborates impressions

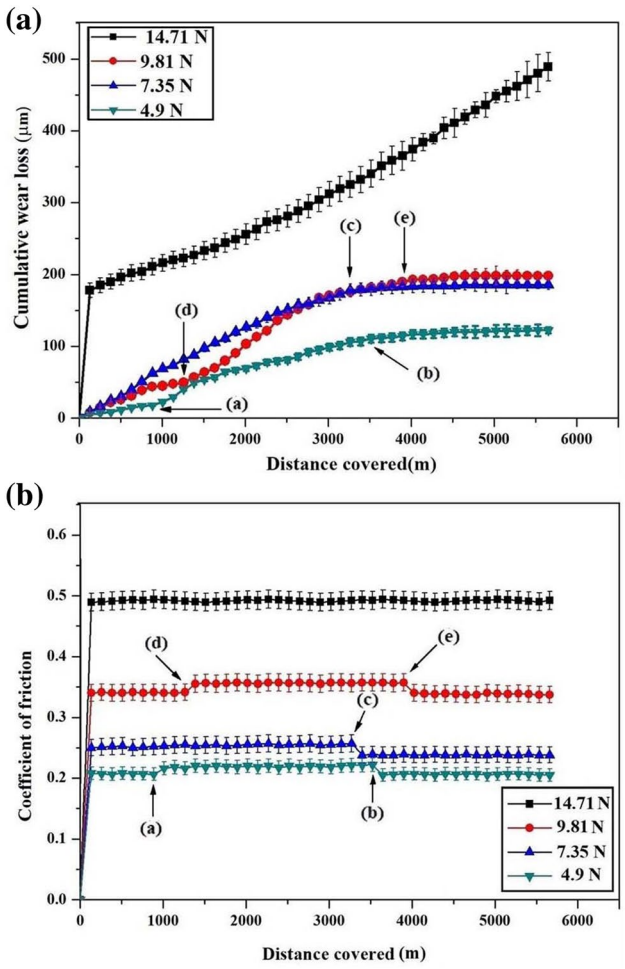

Fig. 9 Wear test results for ITC-4Cy showing (**a**) cumulative wear loss and (**b**) coefficient of friction

of abrasion and broken oxide layer (Fig. 7a). In particular, microplowing effect and oxide dislodgement are identified (Fig. 7b and c). It is quite apparent that on load increment to 14.71 N, abrasive wear removes surface oxide, resulting in a continuous wear loss. The FESEM micrograph and EDS spectra of dislodged oxide are shown in Fig. 7c and d.

The FESEM micrographs of worn debris for annealed AISI 1010 steel at different loads are presented in Fig. 8a–f. At lowest load (4.9 N), the worn debris consists of metal sheets, metal chips, metallic threads, and small fragmented oxide particles (Fig. 8a). Sheets of metal indicate the action of adhesive wear, while metal chips are the outcome of microcutting abrasion. Metallic threads are originated through drilling effect of soft α-ferrite matrix. Particles of oxide in debris are generated through removal of nonadherent layer of oxide. It is important to note that, by virtue of charging effect, oxide particle/layer appears brighter, either on worn surface or in the worn debris. With further increase in load to 7.35 N, features similar to those at 4.9 N are again observed in worn debris, though sizes appear to be bigger due to application of relatively higher load (Fig. 8b). At still higher load (9.81 N), thicker metal sheets, metal chips, oxide fragments, and metallic threads are observed (Fig. 8c and d). Thicker metal sheets are originated through microplowing action of abrasive wear, while metal chips and oxide fragments are evolved due to microcutting action of abrasive wear at relatively higher load (9.81 N). Besides, metallic threads are originated through drilling effect. Furthermore, thicker metal sheets often include lamellar pearlite (harder microconstituent) as identified at higher magnification in terms of lamellar morphology (Fig. 8d). This indicates the removal of harder microconstituent (pearlite) under higher load (9.81 N), thereby further substantiating the relatively higher rate of wear loss up to point 'c' (Fig. 3a) as compared to lower loads (4.9 and 7.35 N). At highest load (14.71 N), debris comprises thin metal chips (generated by microcutting abrasion), thick metal sheets (originated through microplowing abrasion), oxide sheets (removed through microplowing or microcutting abrasion) and metallic threads (Fig. 8e). The FESEM-based EDS spectra of an oxide sheet removed at 14.71 N load are shown in Fig. 8f. Therefore, at higher loads, abrasive wear takes the prime role in the damage of material surface.

Tribological Damage in the Steel Subjected to Intercritical Thermal Cycling

Wear behavior of ITC-4Cy at lowest load (4.9 N) exhibits a steady tribological damage at relatively slower rate till point 'a' and subsequent rise in damage till point 'b' and a final stoppage of wear (Fig. 9a). In accordance, the COF increases between point 'a' and 'b' and thereafter drops down (Fig. 9b). The overall surface after wear test exhibits prominent features of adhesive wear along with abrasive wear and oxide layer (Fig. 10a). Localized oxidation, crack nucleation and metal sheet removal are evident in the adhesion zone (Fig. 10b). Afterward, till point 'a', owing to conjoint action of adhesion and abrasion, the material corroborates a continuous steady tribological damage. However, the tribological surface damage is relatively sluggish by virtue of initial development of oxide on pin surface. Beyond point 'a', oxide is eventually removed through abrasion that results in accelerated wear loss till point 'b' (Fig. 10c). Beyond point 'b', the generation of massive oxide layer (Fig. 10d), owing to environmental reaction augmented by frictional heating, finally arrests the wear loss. The evidence of the

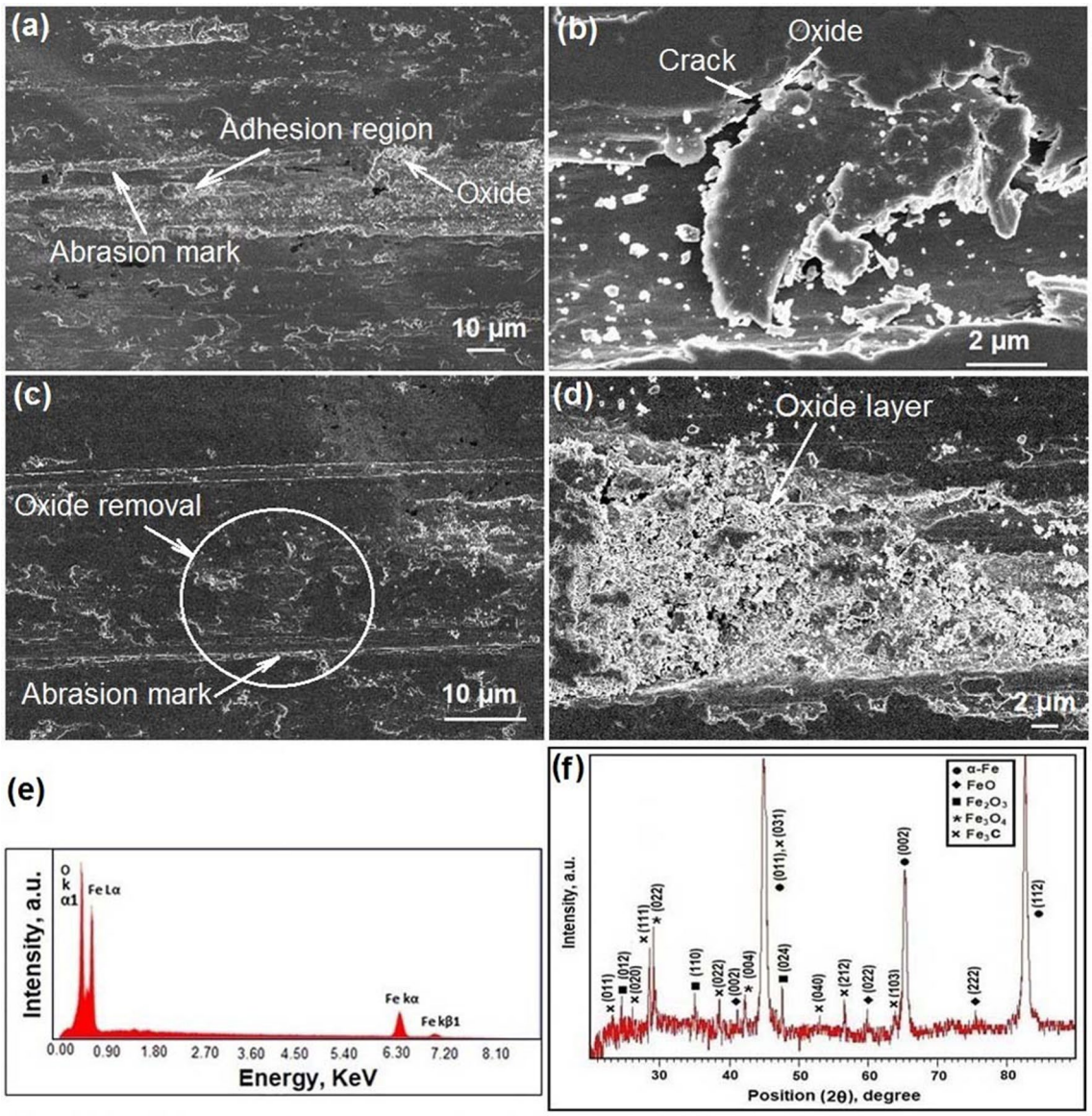

Fig. 10 FESEM micrographs of the worn surface of ITC-4Cy subjected to 4.9 N load: (**a**) overall appearance; (**b**) adhesion region; (**c**) abrasive action; (**d**) adherent oxide layer and its (**e**) EDS spectra; and (**f**) XRD analysis of worn surface

presence of iron oxide is exemplified with its EDS analysis (Fig. 10e) and XRD analysis (Fig. 10f) of worn surface.

At next higher load (7.35 N), the CWL versus SD plot (shown in Fig. 9a) exhibits an initial stage of continuous wear loss up to point 'c' followed by an arrest in wear loss. Accordingly, COF decreases beyond point 'c' (Fig. 9b). The gross micrograph of pin surface corroborates abrasion marks, adhesive zone and oxidation (Fig. 11a). In adhesive zone, the characteristic features, such as oxide evolution, crack nucleation, and delamination, are readily observed (Fig. 11b). Therefore, the simultaneous effects of adhesive and abrasive damages result in a steady tribological damage up to point 'c'. Beyond point 'c', owing to frictional heating, massive oxide layer originates (Fig. 11c) that arrests wear loss.

At 9.81 N, the CWL versus SD graph (Fig. 9a) exhibits an initial stage of continuous slow wear loss up to point 'd'. This is followed by an enhanced rate of wear loss up to point 'e' and finally an arrest in wear loss. In concurrence, COF remains almost unchanged till point 'd' and

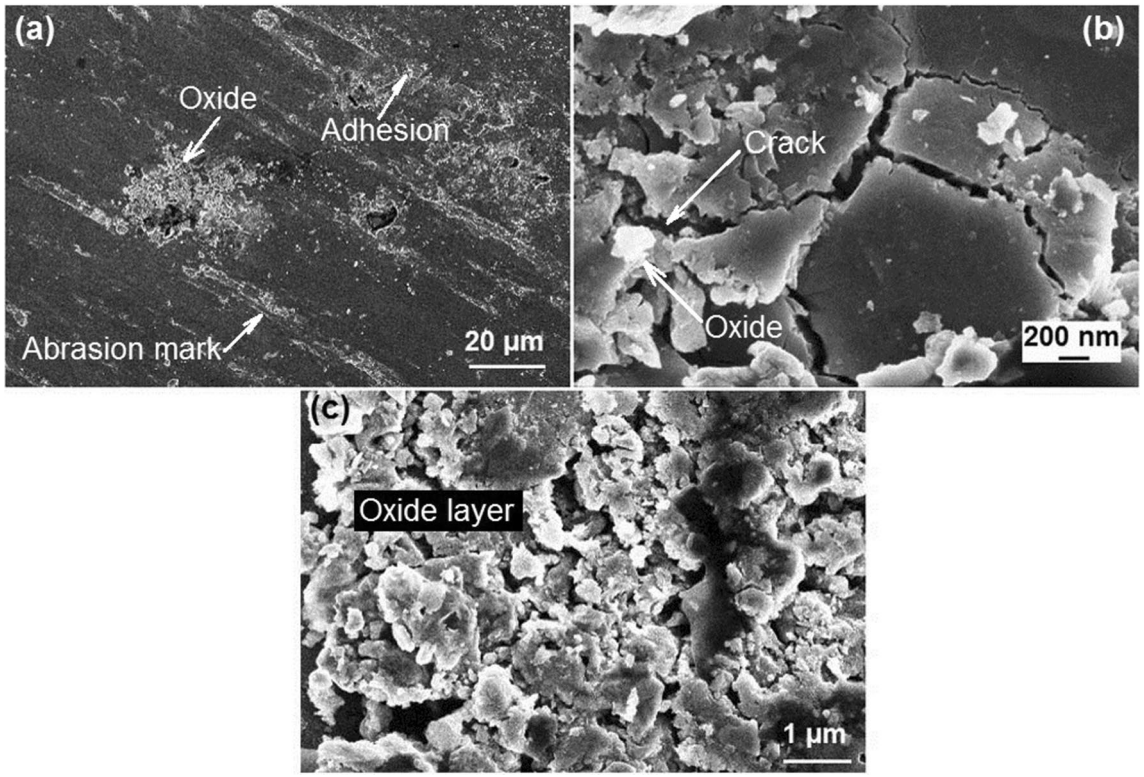

Fig. 11 FESEM micrographs of the worn surface of ITC-4Cy subjected to 7.35 N load: (**a**) overall appearance; (**b**) adhesion region; and (**c**) massive oxide layer generation

henceforth increases up to point 'e' followed by a decline (Fig. 9b). The gross micrograph of pin surface corroborates oxide layer and adhesive zone as well as abrasion marks (Fig. 12a). In adhesive zone, oxide evolution, crack nucleation, and delamination are necessarily observed (Fig. 12b). The concomitant effects of adhesive wear and microcutting abrasion result in a steady tribological damage till point 'd,' though with a slow progress due to the presence of oxide layer. Thereafter, oxide is eventually removed through abrasion (Fig. 12c) resulting in accelerated wear loss from point 'd' to 'e' (Fig. 9a). Adherent oxide (Fig. 12d) originates on pin surface beyond point 'e' (owing to frictional heating) so as to arrest the wear loss. The presence of oxide layer is further confirmed with its EDS spectra (Fig. 12e) and XRD analysis of the worn surface (Fig. 12f).

The CWL versus SD graph at peak load (14.71 N) exhibits a steady but accelerated tribological damage throughout (Fig. 9a). Accordingly, COF remains almost constant with a high value (Fig. 9b). The gross micrograph of surface corroborates prominent abrasion marks and dislodged oxide particles (Fig. 13a). Furthermore, FESEM micrograph at higher magnification (Fig. 13b) corroborates significant microplowing abrasive wear removing surface material (metallic matrix as well as oxide) forming ditches. Therefore, at highest load significant effect of microplowing abrasion envisages a steady accentuated wear.

The FESEM micrographs (Fig. 14a–e) of worn debris of ITC-4Cy can be correlated with worn surface micrographs analyzed above in correlation with that for AN. In particular, at the peak load (14.71 N), metal chips (corroborating microcutting abrasion), thicker metal sheets (indicating microplowing abrasion), fragments of oxides and metal thread (enumerating drilling effect) are observed in debris (Fig. 14d). Furthermore, the EDS spectra of removed oxide fragment (at 14.71 N load) are shown in Fig. 14e.

Surface Strain Hardening and Thermal Softening

Results of microhardness test are corroborated in tabular form (Table 1) as well as graphically (Fig. 15). With regard to initial matrix hardness, an increment in hardness value of the matrix is observed after wear test almost in all the specimens. Furthermore, microhardness value of the worn surface matrix increases with increasing wear test load, except

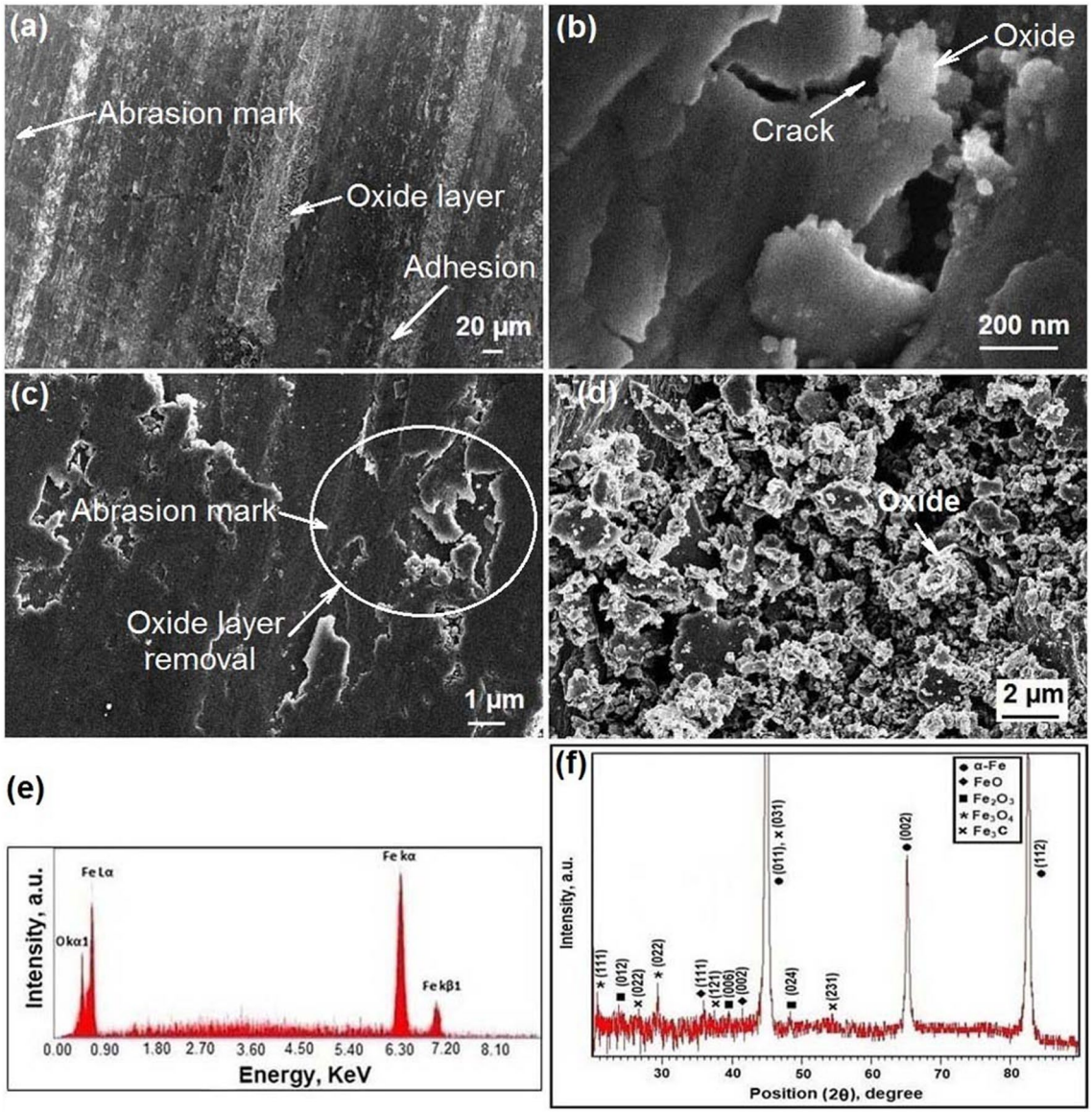

Fig. 12 FESEM micrographs of the worn surface of ITC-4Cy subjected to 9.81 N load: (**a**) overall appearance; (**b**) adhesion region; (**c**) oxide layer removal through abrasion; (**d**) evolution of adherent oxide layer; (**e**) EDS spectra of oxide layer; and (**f**) XRD analysis of worn surface

ITC-4Cy at highest load (14.71 N). The increase in surface hardness after wear test with respect to initial hardness and with increasing load envisages the strain hardening effect in majority of cases. Indeed, concomitant occurrence of strain hardening and thermal softening during tribological tests under load has been reported [25–28]. Detailed analysis on temperature rise due to frictional heating is available in earlier research work carried out by the research group of the present corresponding author [24]. While surface hardness is expected to rise up owing to strain hardening effect, thermal softening effect would reduce the hardness. It appears that, in case of ITC-4Cy at 14.71 N load, thermal softening effect dominates strain hardening effect. This is further substantiated with the existence of tempered martensite and tempered cementite on worn surface of the said specimen (Fig. 16a–c). This envisages the thermal softening effect in the form of tempering of martensite which eliminates the 'lath' or 'plate' morphology of martensite (Fig. 16b). Besides, the cementite particles present in α-ferrite island are also found to be grown into larger size (size range: 115–366 nm) (Fig. 16c).

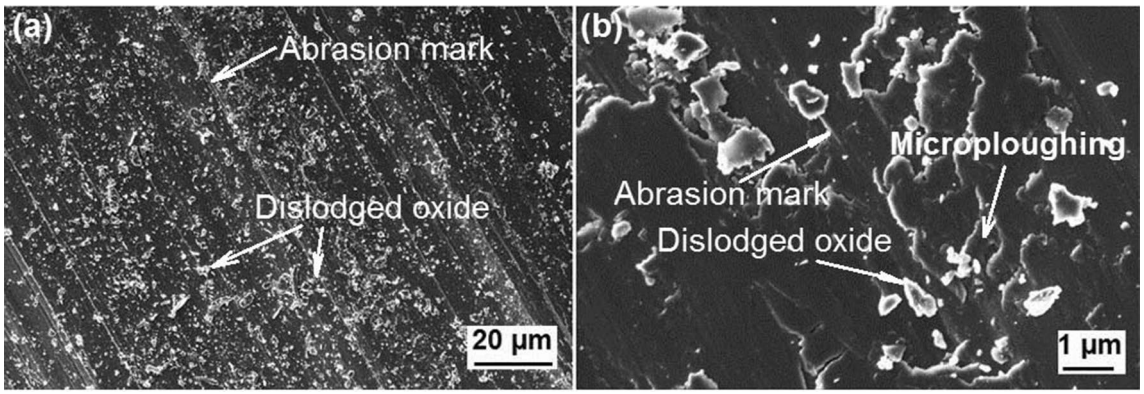

Fig. 13 FESEM micrographs of the worn surface of ITC-4Cy subjected to 14.71 N load: (**a**) overall appearance; (**b**) microplowing effect

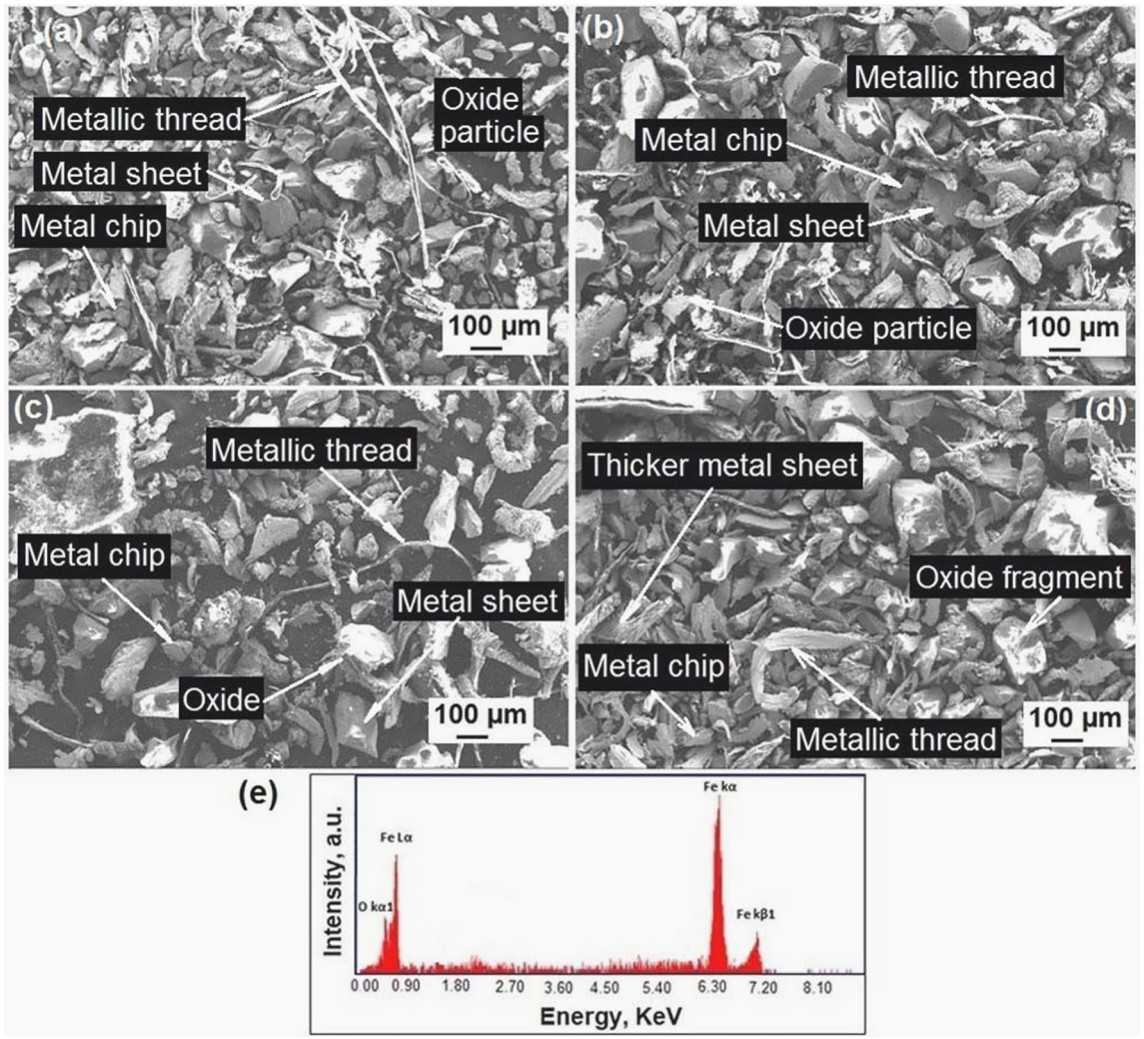

Fig. 14 FESEM micrographs of the worn debris of ITC-4Cy at different loads, namely (**a**) 4.9 N, (**b**) 7.35 N, (**c**) 9.81 N and (**d**) 14.71 N; (**e**) FESEM-based EDS spectra of oxide fragment (14.71 N)

Table 1 Microhardness test results

Specimen code	Microhardness of matrix (mean ± standard deviation), HV				
	Before wear test	After wear test			
		At 4.9 N	At 7.35 N	At 9.81 N	At 14.71 N
AN	119 ± 3 (α-ferrite matrix)	134 ± 2	139 ± 2	147 ± 2	157 ± 2
ITC-4Cy	509 ± 7 (bulk matrix of dispersed cementite in lath martensite)	517 ± 13	523 ± 10	533 ± 24	473 ± 10

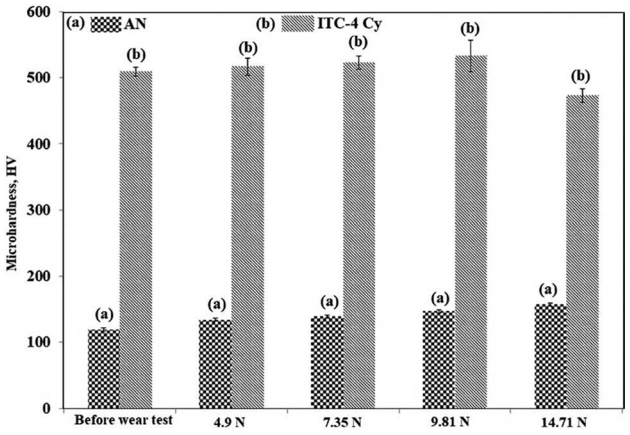

Fig. 15 Matrix microhardness before and after wear test

In case of AN at 14.71 N load, significant presence of strained (thereby often elongated) α-ferrite grains substantiates the strain hardening effect (Fig. 16d).

Overall Tribological Damage

The gross tribological damage (in terms of rate of wear) versus normal load is presented in Fig. 17. Overall, in both kinds of heat treatment conditions, a rise in overall wear rate is observed with normal load. However, for annealed steel (AN), an enhanced wear rate is observed than the steel subjected to intercritical thermal cycling (ITC-4Cy), except at highest load (14.71 N). In annealed steel, the wear rate versus normal load shoots up even at lower loads due to severe abrasive wear (in the form of microcutting and microplowing) which readily

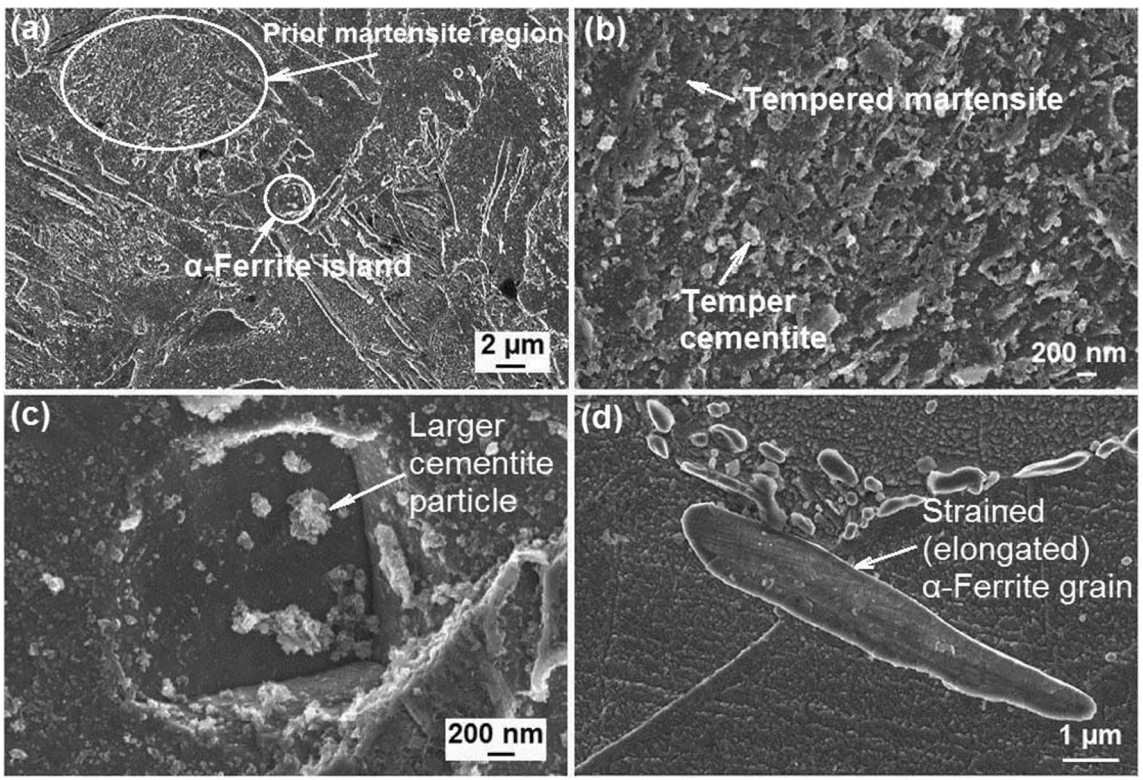

Fig. 16 FESEM micrographs of polished and etched worn surface exhibiting the effect of strain hardening in (**a**) ITC-4Cy (14.71 N)-overall microstructure; (**b**) ITC-4Cy (14.71 N)-tempered martensite region; (**c**) ITC-4Cy (14.71 N)-coarsening of cementite particles in α-ferrite island; (**d**) AN (14.71 N)-Strained α-ferrite grain

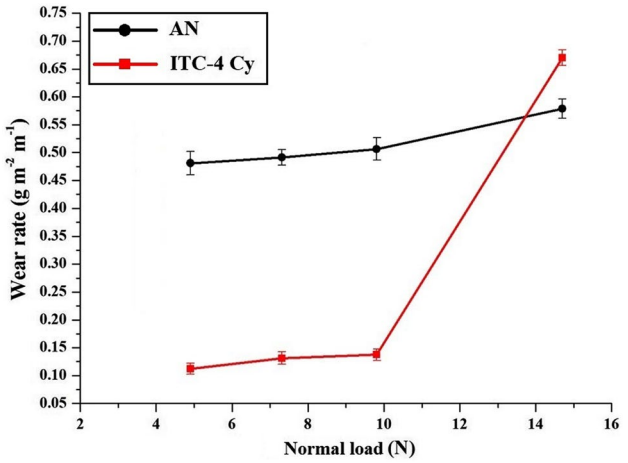

Fig. 17 Variation in overall wear rate with normal load

eliminates surface oxide layer. Such an aggravated wear loss is not experienced for ITC-4Cy up to 9.81 N load. However, for ITC-4Cy, the overall wear rate abruptly increases at highest load (14.71 N) and shoots up even above that of AN. This is due to softening effect in the form of tempering coupled with elimination of oxide layer through microplowing mechanism of abrasive wear, as introspected earlier (Figs. 13b and 16a–c).

Conclusion

(1) At lower load, dry sliding tribological damage in AISI 1010 steel, on a gross scale, is associated with adhesive wear and microcutting-type abrasive wear. On the other hand, microcutting- as well as microplowing-type abrasive wear and oxidation are dominant at higher load. Besides, strain hardening effect is also evident except ITC-4Cy at 14.71 N.

(2) In general, an increase in load raises overall wear rate. Annealed steel (AN) shows an aggravated wear loss and much inferior wear resistance with respect to the steel subjected to intercritical thermal cycling (ITC-4Cy), except at highest load (14.71 N).

(3) In case of AN, elimination of nonadherent oxide layer is quite evident. The harder pearlite regions are also abraded away under higher load. These effects result in higher wear loss in AN.

(4) The intercritical thermal-cycled steel (ITC-4Cy) exhibits much lower wear loss, except at peak load (14.71 N). The softening effect in the form of tempering coupled with microplowing abrasion at highest load (14.71 N) results in an aggravated wear loss in ITC-4Cy. However, up to 9.81 N load, it provides better wear resistance than AN.

References

1. V.D. Eisenhuettenleute, *A Handbook for Materials Research and Engineering*, Ch C4 (Springer, Verlag StahleisenmbH, 1993), p. 78
2. N. Prasad, S.D. Kulkarni, Relations between microstructure and abrasive wear of plain carbon steel. Wear **63**, 329–338 (1980)
3. M.A. Moore, The relationship between the abrasive wear resistance, hardness and microstructure of ferritic materials. Wear **28**, 59–68 (1974)
4. J. Larsen-Badse, K.G. Mathew, Influence of structure on the abrasion resistance of a 1040 steel. Wear **14**, 199–206 (1969)
5. S. Gunduz, R. Kacar, H.S. Soykan, Wear behaviour of forging steels with different microstructure during dry sliding. Tribol. Int. **41**, 348–355 (2008)
6. C.C. Viafara, M.I. Castro, J.M. Velez, A. Toro, Unlubricated sliding wear of pearlitic and bainitic steels. Wear **259**, 405–411 (2005)
7. T.F.J. Quinn, An experimental study of the thermal aspects of sliding contacts and their relation to the unlubricated wear of steel, in *Proceedings of the Institute of the Mechanical Engineers, Conference Proceedings*, vol 183 (1968) p. 129
8. T.F.J. Quinn, The division of heat and temperature at sliding steel interfaces and their relation to oxidational wear. ASLE Trans. **21**, 78–86 (1978)
9. Y.C. Lin, S.W. Wang, T.M. Chen, A study on the wear behavior of hardened medium carbon steel. J. Mater. Process. Technol. **120**, 126–132 (2002)
10. K.M. Lee, A.A. Polycarpou, Wear of conventional pearlitic and improved bainitic rail steel. Wear **259**, 391–399 (2005)
11. L. Xu, N.F. Kennon, A study of the abrasive wear of carbon steels. Wear **148**, 101–112 (1991)
12. J. Kalousek, D.M. Fegredo, E.E. Laufer, The wear resistance and worn metallography of pearlite, bainite and tempered martensite rail steel microstructures of high hardness. Wear **105**, 199–222 (1985)
13. X.Y. Feng, F.C. Zhang, Z.N. Yang, M. Zhang, Wear behaviour of nanocrystallised Hadfield steel. Wear **305**, 299–304 (2013)
14. R.S. Godse, S.H. Gawand, A.A. Keste, Tribological behavior of high fraction carbon steel alloys. J. Bio TriboCorros. **2**(3), 2–9 (2016)
15. R. Autay, M.K. Chaou, F. Dammak, Friction and wear behaviour of induction hardened ISO 42CrMo4 low-alloy steel under reciprocating sliding conditions. Proc. Inst. Mech. Eng. J. **229**(2), 115–125 (2015)
16. L. Zhang, Y. Jin, X. Wang, J. Cai, Q. Guan, Surface alloys of 0.45 C carbon steel produced by high current pulsed electron beam. High Temp. Mater. Proc. **38**, 444–451 (2019)
17. A.N.M. Idriss, M.A. Maleque, I.I. Yaacob, R.M. Nasir, S. Mridha, T.N. Baker, Wear behaviour at 600 °C of surface engineered low-alloy steel containing TiC particles. Mater. Sci. Technol. **33**, 1688–1695 (2017)
18. F.H. Lang, A. Habibolahzadeh, M.H. Sohi, Comparative tribological studies of duplex surface treated AISI 1045 steels fabricated by combinations of plasma nitriding and aluminizing. Mater. Des. **60**, 580–586 (2014)
19. K.W. Andrews, Empirical formulae for the calculation of some transformation temperatures. J. Iron Steel Inst. Jpn. **203**, 721–727 (1965)
20. J.F. Shackelford, W. Alexander (eds.), *Materials Science and Engineering Handbook*. (CRC press, Boca Raton, 2001), p. 473
21. Y.L. Tian, R.W. Kraft, Mechanisms of pearlite spheroidisation. Metall. Trans. A **18**, 1403–1414 (1987)
22. J. Maity, A. Saha, D.K. Mondal, K. Biswas, Mechanism of accelerated spheroidization of steel during cyclic heat treatment around

the upper critical temperature. Philos. Mag. Lett. **93**, 231–237 (2013)
23. K.L. Sahoo, C.S.S. Krishnan, A.K. Chakrabarti, Studies on wear characteristics of Al–Fe–V–Si alloys. Wear **239**, 211–218 (2000)
24. M.K. Mondal, K. Biswas, J. Maity, A transient heat transfer model for assessment of flash temperature during dry sliding wear in a pin-on-disk tribometer. Mater. Trans. A **47A**, 600–607 (2016)
25. J. Zhang, A.T. Alpas, Transition between mild and severe wear in aluminium alloys. Acta Mater. **45**, 513–528 (1997)
26. S.C. Lim, M.F. Ashby, Overview no. 55 wear-mechanism maps. Acta Metall. **35**, 1–24 (1987)
27. W. Hirst, J.K. Lancaster, The influence of speed on metallic wear. Proc. R. Soc. A **259**, 228–241 (1960)
28. N. Saka, A.M. Eleiche, N.P. Sub, Wear of metals at high sliding speeds. Wear **44**, 109–125 (1977)